

Identification of Aerodynamic Models for an Energy-Harvesting Kite using Multisine Inputs and Equation Error

Diaa A. Zekry*

Princeton University, Princeton, NJ, 08544, USA

Taewoo Nam[†] and Yufei Zhu[‡]
Toyota Research Institute of North America, Ann Arbor, MI, 48103, USA

Aimy A. Wissa[§]
Princeton University, Princeton, NJ, 08544, USA

System identification (SysID) techniques were applied to nonlinear simulation data for Toyota's Airborne Wind Energy Harvesting (AWEH) kite with bioinspired control effectors to develop accurate aerodynamic models. Orthogonal phase-optimized multisine inputs were designed to simultaneously excite all four bio-inspired control surfaces. Aerodynamic forces and moments were reconstructed using a modified flight dynamics model, accounting for bridle tension effects inherent to the tethered kite configuration. Stepwise regression and the equation-error approach were used to determine the aerodynamic model structure and estimate nondimensional stability and control derivatives. The results highlight the successful analysis of this type of airborne energy harvesting system, laying a foundation for flight testing and further refinement of aerodynamic and control models for AWEH systems. Additionally, the paper explores interesting aspects of identifying the aerodynamics of cable-tethered kites.

Keywords: system identification, multisines, equation error, flight dynamics, energy harvesting, kite

Nomenclature

 A_k , Φ_k = multisine amplitude and phase angle, rad

b = wing span, m

 \bar{c} = mean aerodynamic chord, m

C_X, C_Z, C_m = body-axis nondimensional longitudinal aerodynamic force and moment coefficients

F = external force vector acting on the kite, N I = kite mass moment of inertia matrix, kg-m²

m = kite mass, kg

M = external moments vector acting on the kite, N-m

p, q, r = body-axis roll, pitch, and yaw rates, rad/s

 \mathbf{r}_{1CG} , \mathbf{r}_{2CG} = position vector of LE and TE bridle line connection point from kite CG, respectively, m

R² = coefficient of determination

t = time, s

T = total maneuver duration, s

 \mathbf{V} = body-axis linear velocity vector $[\mathbf{v}_{x}, \mathbf{v}_{y}, \mathbf{v}_{z}]^{\mathrm{T}}$, m/s

 V_{∞} = free-stream true airspeed, m/s

 α = angle of attack, rad β = sideslip angle, rad

ω = body-axis angular velocity vector [p, q, r]^T, rad/s

^{*}PhD Candidate, Mechanical and Aerospace Engineering at Princeton University, Princeton, NJ, 08544, USA, AIAA Member.

[†]Senior Research Manager, Toyota Research Institute of North America, Ann Arbor, MI, 48103, USA.

[‡]Research Engineer, Toyota Research Institute of North America, Ann Arbor, MI, 48103, USA.

[§] Assistant Professor, Mechanical and Aerospace Engineering at Princeton University, Princeton, NJ 08544, USA, AIAA Member.

Subscripts

A = aerodynamic force or moment

CG = center of gravity

G = gravity force or moment
0 = reference value or bias term
T = tension force or moment
1 = LE connection point to kite
2 = TE connection point to kite

 ∞ = free-stream

Superscripts

Acronyms

LE = leading edge TE = trailing edge

I. Introduction

Wind energy harvesting has become increasingly important in the last decade because it can provide a sustainable alternative to fossil fuels and help mitigate the effects of climate change. Conventional wind energy farms are ground-based, which limits the energy available for extraction to wind close to the ground. Thus, this wind is in the boundary layer of the Earth and, consequently, has less energy than other winds at higher altitudes. Ground-based systems also require high-cost infrastructure investments, such as base towers, which increase costs and environmental impact [1]. Airborne Wind Energy Harvesting (AWEH) is an air-based system that uses tethered kites to generate energy at high altitudes utilizing the increased wind velocity (e.g., jet streams) at these altitudes.

AWEH systems are light, mobile, and multifunctional. Compared to ground-based systems with similar power output, AWEH weighs 20 times less when considering the weight of the wind turbine blades alone and more than 300 times less if the weight of the base tower infrastructure is considered [2]. Examples of AWEH systems include Makani [3], skysails [4, 5], and Toyota's Mothership kite [6–8], which is the subject of this paper. AWEH systems usually generate power using two mechanisms. The first is by turning onboard propellers that operate generators. An example of this system is the Makani kite [3]. The other mechanism is to pull on a tether connected to a ground generator by performing pumping cycles with reel-in and reel-out phases. The reel-out phase is a power generation phase, where the kite flies a high α , high-resistance, cross-wind maneuver. The reel-in phase is a power consumption phase, where the kite flies at low α while being pulled back to the starting position to repeat the cycle. An example of this reel-in / reel-out system is Toyota's Mothership kite [6–8].

AWEH kites are usually lightweight, flexible structures with complex bridle line connections and pitch controllers. In some cases, like the Mothership, the kite has an inflatable tube with a fabric-like surface structure and no empennage. This structural compliance changes the aerodynamic characteristics of the kites and can create difficult control law design and characterization challenges. Previous studies [1, 9–12] present an analysis of the flight dynamics and stability of different examples of kites at different levels of complexity. However, the presented models involved many simplifications and idealizations of physics that are difficult to predict from first principles.

In contrast to first-principles modeling approaches, another approach is system identification (SysID), which involves extracting models from experimental data and known vehicle properties [13]. Aircraft SysID can be useful in designing stability augmentation and flight control systems, along with updating flight simulators. There are multiple techniques for performing SysID, and a recent state-of-the-art review of practical aircraft SysID developments can be found in Ref. [14]. System identification (SysID) has been applied to characterize compliant airborne systems, such as parachutes [15], and flexible aircraft like the X-56A [16]. In AWEH systems, SysID has been utilized to develop and refine control laws based on known aerodynamic properties obtained from wind tunnel experiments or computational fluid dynamics (CFD) analyses [1, 9–12]. Despite the potential of SysID for AWEH systems, there is a notable absence of literature applying SysID to derive realistic aerodynamic models from flight test data. This is particularly true because the desired maneuvers for aerodynamic model identification are complicated and time-consuming and are, therefore, difficult to

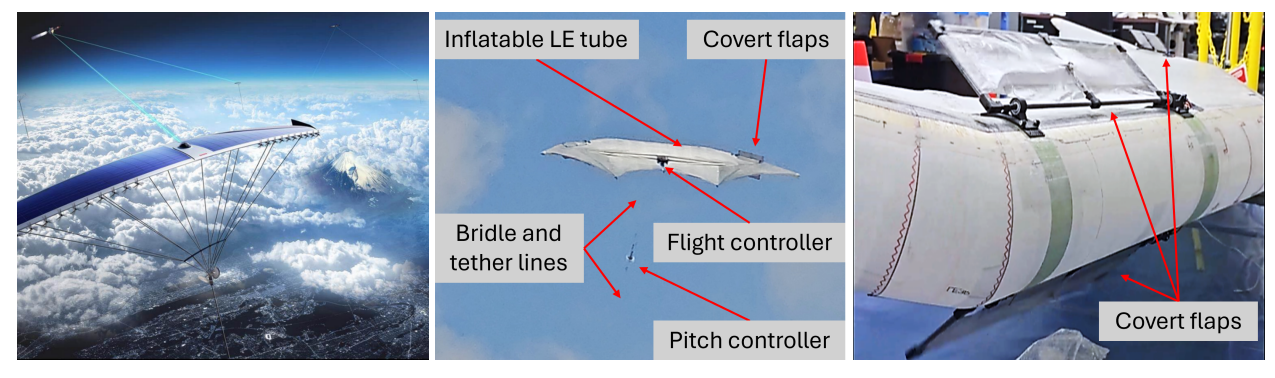
perform during expensive flight tests.

Developing a comprehensive aerodynamic model for Toyota's Mothership kite is essential for stability augmentation and optimizing the pumping cycle maneuvers for efficient energy production, both of which are critical to achieving the kite's mission objectives. This work supports those mission objectives by verifying experiment design and modeling approaches using nonlinear simulation tools before conducting the flight tests. Performing SysID based on simulation tools helps refine the experiment and analysis early and improves the chances of success during flight tests. For the excitations, orthogonal phase-optimized multisines were designed to simultaneously move all four of the bio-inspired control effectors onboard the Mothership kite in an efficient manner that reduced time and costs [13, 16, 17]. Subsequently, equation-error was used, where models of the nondimensional aerodynamic coefficients were determined using a manual stepwise regression procedure. After determining the aerodynamic coefficients, values and uncertainties for the stability and control derivatives were estimated using ordinary least squares approach.

The remainder of the paper is organized as follows. The kite and simulator specifications are described in Section II. A multisine input design is summarized in Section III. Aerodynamic forces and moments, calculated using dynamic equations and sensor measurements, are discussed in Section IV. Nondimensional mathematical equations of the aerodynamic coefficients are derived and discussed in Section V.

II. Mothership Design Overview

Figure 1a shows an artist's rendering of Toyota's Mothership project [18, 19], which is a futuristic, high-altitude AWEH system projected to fly at altitudes exceeding 10 km. It is a multifunctional platform facilitating atmospheric data acquisition, satellite communication, and wind energy harvesting. As part of the research and development efforts, a scaled-down version, shown in Fig. 1b, has been simulated and manufactured for future testing.



(a) Artist impression of Toyota's Mother-(b) Proof of concept kite with covert flaps (c) Close-up of the colocated LE covert ship kite [6] for flight control flaps

Fig. 1 Toyota's Mothership kite concept and proof of concept.

The scaled-down kite has two inflatable tube structures with fabric extended over the top, giving the wing its shape and structure. The wing span is 5.75 m, the mean aerodynamic chord is 0.978 m, and the wing area is 6 m². For flight control, the kite has four feather-inspired flap surfaces. Two are on the left (port) side of the wing, and two are on the right (starboard) side, shown in Fig. 1c. On each side, one flap is located on the upper surface and the other on the lower surface of the wing, both positioned at the same spanwise and chordwise locations. The flaps are mounted on the leading-edge inflatable tube structure of the kite, resulting in effective deflections opposite to those of conventional trailing-edge aircraft flaps. For instance, a deflection of the leading edge upper surface flaps has the same effect on the pitching moment coefficient as a conventional trailing edge pressure side flaps. Hence, flap deflection convention is defined as positive upward for suction-side flaps and negative downward for pressure-side flaps. The flaps are denoted using the Greek letter δ , with subscripts r or 1 indicating the right or left sides, respectively, and t or b denoting the top or bottom surfaces. The flaps are inspired by a group of feathers known as the covert feathers. More details about the coverts as flow and flight control devices can be found in Refs. [20–25]. The kite is connected by bridle lines to a pitch control unit, which is tethered to the ground station through the main tether line. While the ultimate goal of the project is to achieve a 10 km altitude, the current system is designed for initial testing at a more practical altitude of approximately 150 m.

The kite is equipped with a custom flight data computer. It has an inertial measurement unit (IMU) that provides tri-axial gyroscope and accelerometer outputs and a global positioning system (GPS) module. The data is sampled at a rate of 100 Hz. The flaps are controlled by servo motors with position feedback. Since the flight velocity and aerodynamic loads on the flaps are small compared to the servo specifications, the actual deflection angles of the control surfaces are assumed to be the servo output shaft angles provided by the feedback. Additionally, the kite is equipped with an extended-range Endurance micro air data computer and a five-hole probe from Aeroprobe Corporation for airspeed, altitude, angle of attack, and sideslip angle measurements [26]. Finally, a multi-axis load cell was mounted on the tether line to measure the tension. The total kite mass with instrumentation is less than 5 kg. Table 1 shows the kite geometry and nominal mass properties.

Table 1	kite geometr	v and nominal	l mass pro	perties

Parameter	Estimate	Units		
ē	0.978	m		
b	5.75	m		
S	6	m^2		
m	4.1	kg		
I_{xx}	6.9	kg-m ²		
I_{yy}	0.841	kg-m ²		
I_{zz}	7.6	kg-m ²		
I_{xz}	0	kg-m ²		

A dynamic model of the kite system was created using MapleSimTM simulator by Maple Corporation, a commercial Modelica-based simulation package. A combination of available libraries and individual component mass properties, kinematic constraints, and external forces was used to derive the equations of the kite motion.

The MapleSim kite model was treated as a six Degree of Freedom (DoF) system with aerodynamic coefficients as input from wind tunnel and computational fluid dynamics (CFD) experiments. The tether was discretized and modeled as point masses and linear compliant connections to account for the tether inertia and wind forces. More details about the kite and nonlinear simulation can be found in Refs. [6, 8, 12, 27].

III. Experimental Design

The primary objective of the experimental design is to excite the dynamics of interest and gather data with sufficient information content for an accurate system identification analysis while staying within practical constraints such as time and cost. Orthogonal phase-optimized multisines [13, 16, 17, 28–30] are excitations where each control surface input is the sum of harmonic phase-shifted sinusoids of the form

$$\delta_{j} = \sum_{k \in K_{j}} A_{k} \sin \left(\frac{2\pi kt}{T} + \Phi_{k} \right) \tag{1}$$

for j=1,2,...,4. The integer k is the harmonic number, and the sets K_j contain the harmonic numbers for the harmonic sinusoids applied to each control surface. The amplitude spectrum A_k is designed to emphasize or deemphasize specific frequency components. The phase angles Φ_k are optimized for each input to yield minimum relative peak factors. Optimizing the phase angles in this way helps to produce small perturbation responses that are good for linear modeling. More information on multisine design can be found in Refs. [13, 28]. The NASA software called System IDentification Programs for AirCraft (SIDPAC) [31] was used to construct these excitations.

Multisines are useful in SysID because they can cover a wide frequency band and are orthogonal in both the time and frequency domains. Since all sinusoidal components are mutually orthogonal, different harmonics can be assigned to different control surfaces, which allows simultaneous deflection of each control surface. This simultaneous deflection allows the models to capture the interactions between the control surfaces and reduces testing time while maintaining low input correlation [13]. Furthermore, because the excitations are added at the actuator commands, the effects of data collinearity are reduced, even with a control law active.

Multiple groups of maneuvers were designed for model identification and validation. Each maneuver was executed once the kite reached steady-state flight conditions. For the modeling dataset, a maneuver length $T=20\,\mathrm{s}$ was chosen, corresponding to a fundamental frequency of 0.05 Hz and a frequency resolution of 0.05 Hz. The analysis presented in this paper utilized a wide-band frequency range of up to 5 Hz, capturing the spread of potential kite modes based on preliminary findings from wind tunnel and CFD simulations. In future flight tests, the frequency range of interest may be reduced as data are collected.

The kite configuration and the bio-inspired coverts introduced unique considerations compared to traditional aircraft and control surfaces. Unlike conventional systems, the flaps are mounted on top of the wing surface. Hence, the suction side flaps can only deflect upward (positive deflection), while the pressure side flaps can only deflect downward (negative deflection). The simulation run for model identification had the flaps set at a steady state condition of +30 deg on the suction side and -30 deg on the pressure side before performing the maneuvers. Another unique aspect of the kite compared to traditional aircraft is the selection of multisine amplitudes. For the kite, amplitudes were selected to be up to 30 deg, which had the flaps traverse the full range of allowable deflection. Traditional aircraft typically have deflection amplitudes between 0.5 and 4 deg. This increased amplitude was necessary due to the low operational speed of the kite of 7 m/s and the relatively low control authority of the flaps at low deflection angles. Despite these large deflections, the kite maintained a near steady state condition during maneuvers, with α and β varying within ± 2 deg, and ± 5 deg, respectively, which is typical of maneuvers used for linear modeling. For validation datasets, a 3211 multistep was run on each flap, as well as additional independent sets of multisine maneuvers.

The physical servo limitations were carefully considered during maneuver design to prepare the kite for flight testing in the next project phase. This includes accounting for the difference between the scheduled maneuver and the actual response, servo frequency limitations, and the real achievable deflection angles during flight. Both a ground test and a dry run flight test were conducted to verify that the designed maneuvers were achievable. Figure 2 shows examples of the designed multisine and 3211 excitations.

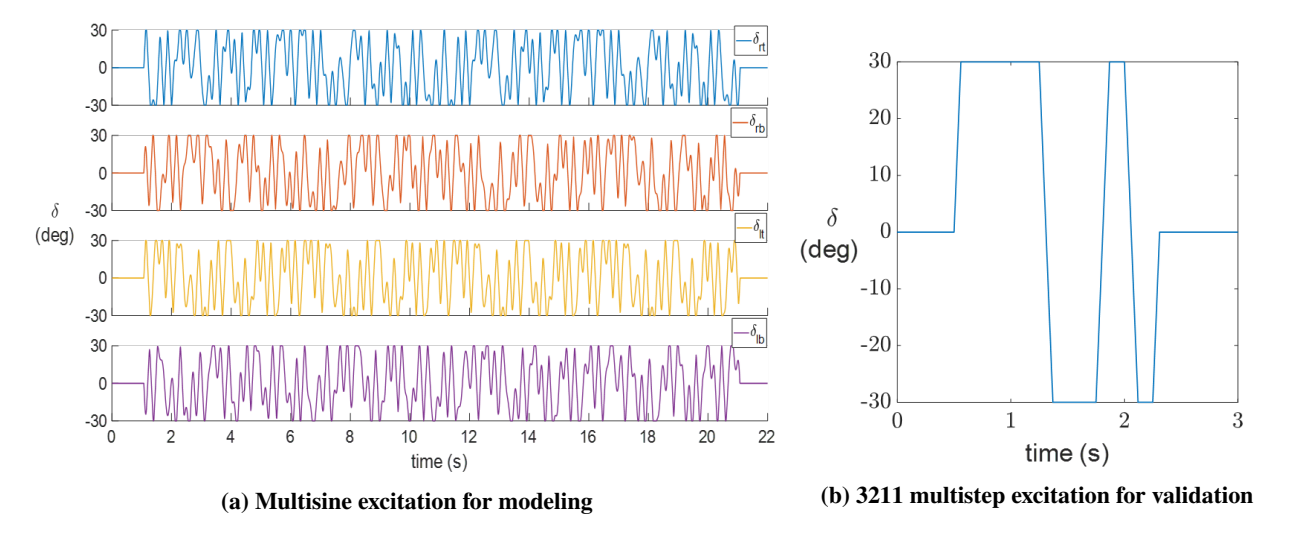


Fig. 2 System identification maneuver.

IV. Measured Aerodynamic Outputs

Equation error parameter estimation is a maximum likelihood estimator that considers process noise in the data. It has numerous advantages, including analytic solutions that are fast to compute, decoupling of the modeling problems for the aerodynamic coefficients, availability of numerous statistical measures for model structure determination, and several others [13]. However, before applying this method, the aerodynamic force and moment coefficients must be accurately measured or reconstructed from measured data using equations of motion (EoM) for the kite. In this section, conventional rigid-body flight dynamics equations of motion are used. Additional terms are introduced to account for the bridle tension lines, which are unique to tethered kite configurations and not encountered with free-flying aircraft. Furthermore, in preparation for flight testing, a Monte Carlo technique is applied to propagate estimated sensor errors through the model. This approach evaluates response sensitivities for each sensor and provides recommendations to

improve measurement accuracy before the actual flight tests.

Figure 3a shows a free-body diagram of the kite with the main forces acting on the kite in flight: aerodynamic forces, gravitational forces, and tension forces from the bridle lines. The kite force and moment equations can be written in the moving, body-fixed kite frame as

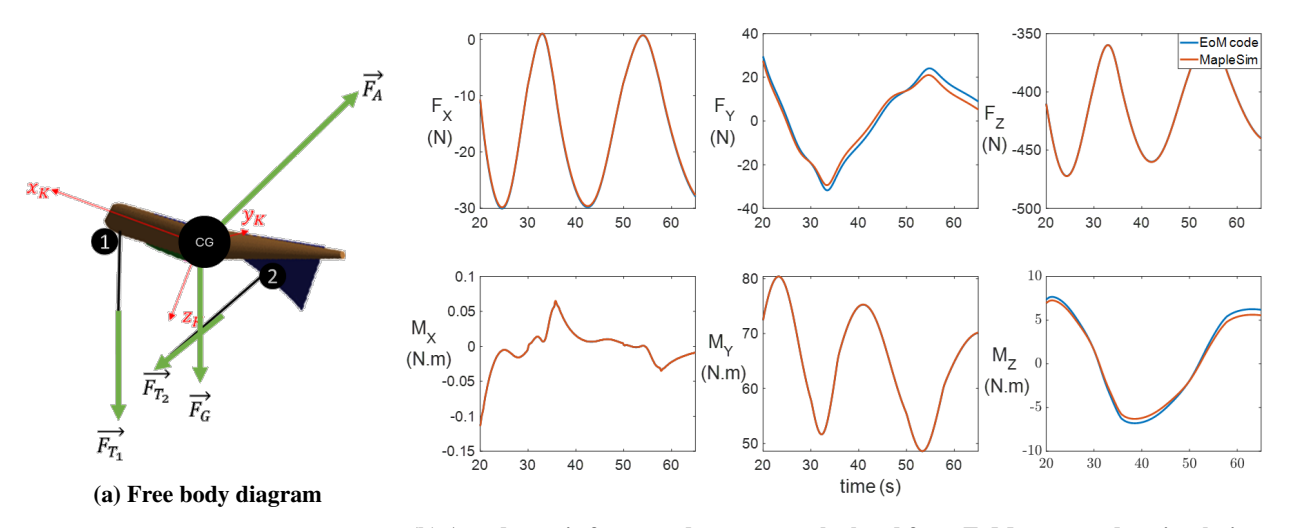
$$\mathbf{F} = \mathbf{m} \left(\dot{\mathbf{V}} + \boldsymbol{\omega} \times \mathbf{V} \right) \tag{2a}$$

$$\mathbf{M} = \mathbf{I}\dot{\boldsymbol{\omega}} + \boldsymbol{\omega} \times (\mathbf{I}\boldsymbol{\omega}) \tag{2b}$$

where the forces and moments in Eq. (2) can be expanded to explicitly show contributions from aerodynamics, gravity, and tension as

$$\mathbf{F} = \mathbf{F}_{\mathbf{A}} + \mathbf{F}_{\mathbf{G}} + \mathbf{F}_{\mathbf{T}} \tag{3a}$$

$$\mathbf{M} = \mathbf{M}_{\mathsf{A}} + \mathbf{M}_{\mathsf{T}} \tag{3b}$$



(b) Aerodynamic forces and moments calculated from EoM compared to simulation

Fig. 3 Free-body diagram and comparison of simulations.

The gravitational force is resolved in the body frame using conventional 3-2-1 Euler angle transformations from the inertial frame to the body frame. The aerodynamic forces are non-dimensionalized using the dynamic pressure and planform area, as well as the characteristic length for the moments. More details about the EoM can be found in [13, 32].

The kite configuration differs from free-flying aircraft due to the presence of bridle lines, which are essential in power generation through the connection to a ground-based generator. The resultant tension force on the kite is calculated as the vector sum of the forces exerted by each individual bridle line Eq. (4a), and the tension moment is calculated using the cross-product of the position vector from the CG to the bridle point connection with the force vector Eq. (4b), as

$$\mathbf{F}_{\mathrm{T}} = \mathbf{F}_{\mathrm{T}_{1}} + \mathbf{F}_{\mathrm{T}_{2}} \tag{4a}$$

$$\mathbf{M}_{\mathbf{T}} = \mathbf{r}_{1\mathbf{C}\mathbf{G}} \times \mathbf{F}_{\mathbf{T}_2} + \mathbf{r}_{2\mathbf{C}\mathbf{G}} \times \mathbf{F}_{\mathbf{T}_2} \tag{4b}$$

Equations (2a) and (2b) form a complete system of equations that were used to calculate the non-dimensional aerodynamic coefficients given the kite mass properties; the free-stream flow conditions; and sensor measurements from accelerometers, gyroscopes, and multi-axis load cells using MATLAB[®].

Figure 3b shows the EoM code prediction versus actual forces from MapleSim for part of the test maneuver. Both the forces and moments show good agreement between the predicted and the actual value with minimal deviations at some points in the side force and yawing moment due to minor errors in the tension vector direction estimation.

A Monte Carlo error propagation study was conducted to evaluate the sensitivity of calculated aerodynamic responses to potential added sensor measurement noise. Sensor errors were modeled as normally distributed random errors,

with parameters based on specifications from each sensor datasheet. All inputs were perturbed simultaneously. In preparation for upcoming flight tests, this analysis identified which sensors most significantly impact the aerodynamic responses, allowing for adjustments in the sensor setup prior to flight testing and tuning of the excitation amplitudes for good predicted signal-to-noise ratios. These adjustments aim to ensure more reliable data collection and improve the accuracy of aerodynamic model estimation in real flight conditions [33].

The results from the error propagation study are shown in Figure 4, where the absolute value of the correlation coefficient for each input with each output is illustrated. High correlations indicate that the estimation of dependencies can become ambiguous and less accurate, hence lower correlations are typically desired. For this set of sensors, even after perturbations the mean of the perturbed value was not statistically different from the true values, meaning that the accuracy of the chosen sensors is sufficient for modeling flight conditions. Figure 4 further supports this observation, demonstrating that all output-input correlations are below 0.2, with the exception of the correlation between T_1 (LE tension) and F_Z (Lift proxy) at 0.28, and between T_1 and M_V (pitching moment) at 0.8.

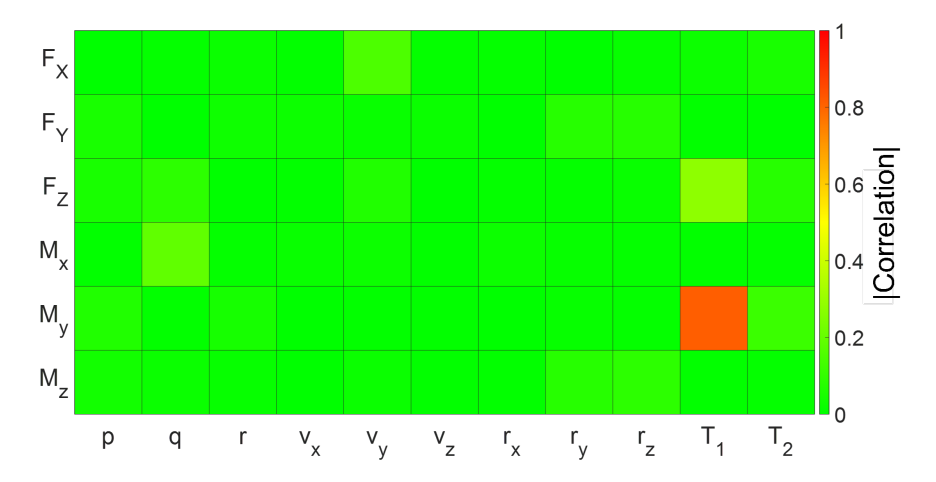


Fig. 4 Input-output correlation coefficients from error propagation study using Monte Carlo simulation

The increased sensitivity of the lift and pitching moment to the LE tension is from the unique characteristics of the tethered kite configuration and the high angle of attack at steady-state conditions. At these high angles, the kite has the tendency to pitch up, exerting a greater pulling force on the LE line compared to the TE line. As a result, the added load in T_1 is directly linked to the pitching moment and z-axis force changes. While all sensors proved sufficient for modeling, it is recommended that the leading edge load cell be replaced with a more accurate sensor to enhance precise modeling in the pitching moment direction.

V. Model Structure Determination and Parameter Estimation

In this section, the functional dependence of the nondimensional aerodynamic coefficients on the airflow angles, angular rates, and control surface deflections is determined. The equation-error approach was used for model identification. Model structure determination was performed iteratively using stepwise regression, and the final stability and control derivatives parameter estimates were determined using ordinary least squares regression. Stepwise regression is an iterative linear regression process involving forward selection and backward elimination [13]. The modeling begins with a bias term, and regressors are added from the pool of postulated candidates. The regressor with the highest correlation to the measured output is retained, and the process continues accordingly with sequentially conditioned data. Early-stage regressors may become redundant as new ones are added, so backward elimination is employed to remove these unnecessary terms. Throughout this process, numerous statistical metrics are monitored to judge model adequacy. One such metric is the coefficient of determination, R², which is a statistical measure that varies from 0 to 1 and indicates the proportion of variance in the response that can be explained by the regressors.

Two pools of candidate regressors were set for this study to derive aerodynamic models of varying complexity. The first focused on deriving a linear model and consisted of all linear terms of the flow angles (α and β), angular rates (p, q, and r), and control surface deflection angles (δ_{rt} , δ_{rb} , δ_{lt} , and δ_{lb}). The second pool contained all possible second-order combinations of the terms in the linear set, incorporating mixed terms such as $\alpha\delta$ as well as second-order powers like α^2 .

The stepwise regression was conducted using JMP[®] statistical software [34], with the minimum Bayesian Information Criterion (BIC) as the stopping criterion. This criterion helped prevent overfitting by limiting the model to only essential regressors. The minimum BIC, which is based on the likelihood function, serves as a means of penalizing the addition of unnecessary terms, ensuring that the final model remains accurate yet not overly complicated.

Both longitudinal and lateral-directional aerodynamic models are presented. The aerodynamic coefficient values used in the presented models are derived from wind tunnel experiments and CFD analyses, which have been used as inputs for the simulator. It is important to note that these values are subject to variation, and actual flight test data may yield different results due to the inherent differences between simulated and real-world conditions. To replicate sensor measurement noise, random, normally distributed noise was added to the sensor measurements. The noise parameters were selected to match those of the sensors currently employed on the kite, ensuring a conservative model derivation. To minimize bias in the parameter estimates due to measurement noise, regressor data were smoothed, as is common practice [13]. The final presented model residuals and errors were assessed for randomness, and the standard errors were adjusted to account for colored residuals [13].

Figure 5 presents the time history of the flow angles, angular rates, and flap deflection angles for a multisine maneuver performed around trimmed flight conditions in the nonlinear simulator. The longitudinal and lateral-directional aerodynamic responses and linear and nonlinear models are displayed in Fig. 5, while the corresponding model residuals are shown in Fig. 6. All the demonstrated models match the responses with small deviations.

The longitudinal linear models had R^2 values of 83%, 89%, and 87% for C_X , C_Z , and C_m , respectively, as shown in Table 2. The lateral-directional linear models had R^2 values of 97%, 78%, and 93% for C_Y , C_1 , and C_n , respectively, as shown in Table 3.

Table 2 Stepwise regression parameter estimation results for the longitudinal body-axis force/moment coefficients - linear model

	0	$\Delta \alpha$	Δβ	q	$\Delta\delta_{ m rt}$	$\Delta\delta_{rb}$	$\Delta \delta_{lt}$	$\Delta \delta_{lb}$	R ²	R ² Validation
C_X	0.101	0.915	-0.075	-	-0.020	-0.013	-0.020	-0.014	0.83	0.93
Standard Error	0.0003	0.0470	0.0115	-	0.0014	0.0011	0.0014	0.0012		
Percent Error	0.29	5.14	15.48	-	7.09	8.35	6.92	8.60		
C_Z	-0.850	-2.421	0.089	-	0.031	-0.020	0.031	-0.019	0.89	0.95
Standard Error	0.0003	0.0525	0.0129	-	0.0015	0.0013	0.0015	0.0013		
Percent Error	0.04	2.17	14.5	-	4.96	6.35	4.95	7.00		
C _m	0.214	0.076	-0.333	-4.256	0.008	-0.007	0.008	-0.011	0.87	0.86
Standard Error	0.0003	0.0465	0.0114	0.3141	0.0014	0.0011	0.0013	0.0012		
Percent Error	0.13	61.52	3.42	7.38	16.98	16.06	16.28	10.54		

Table 3 Stepwise regression parameter estimation results for the lateral-directional body-axis force/moment coefficients - linear model

	0	Δβ	p	r	$\Delta\delta_{ m rt}$	$\Delta\delta_{rb}$	$\Delta \delta_{lt}$	$\Delta \delta_{lb}$	R^2	R ² Validation
C_{Y}	0.000	0.801	-0.095	0.056	-0.004	-0.015	0.003	0.015	0.97	0.98
Standard Error	0.0002	0.0159	0.0246	0.0110	0.0013	0.0010	0.0013	0.0011		
Percent Error	-	1.98	25.77	19.74	33.84	6.70	41.06	7.19		
C_l	0.000	0.078	-0.171	-0.060	0.011	-0.007	-0.011	0.007	0.78	0.74
Standard Error	0.0001	0.0049	0.076	0.0034	0.0004	0.0003	0.0004	0.0003		
Percent Error	-	6.34	4.46	5.75	3.91	4.68	3.83	4.96		
C_n	0.000	0.013	-0.091	-0.071	0.008	0.014	-0.008	-0.015	0.93	0.95
Standard Error	0.0001	0.0050	0.0078	0.0035	0.0004	0.0003	0.0004	0.0003		
Percent Error	-	39.24	8.53	4.91	5.16	2.27	5.15	2.32		

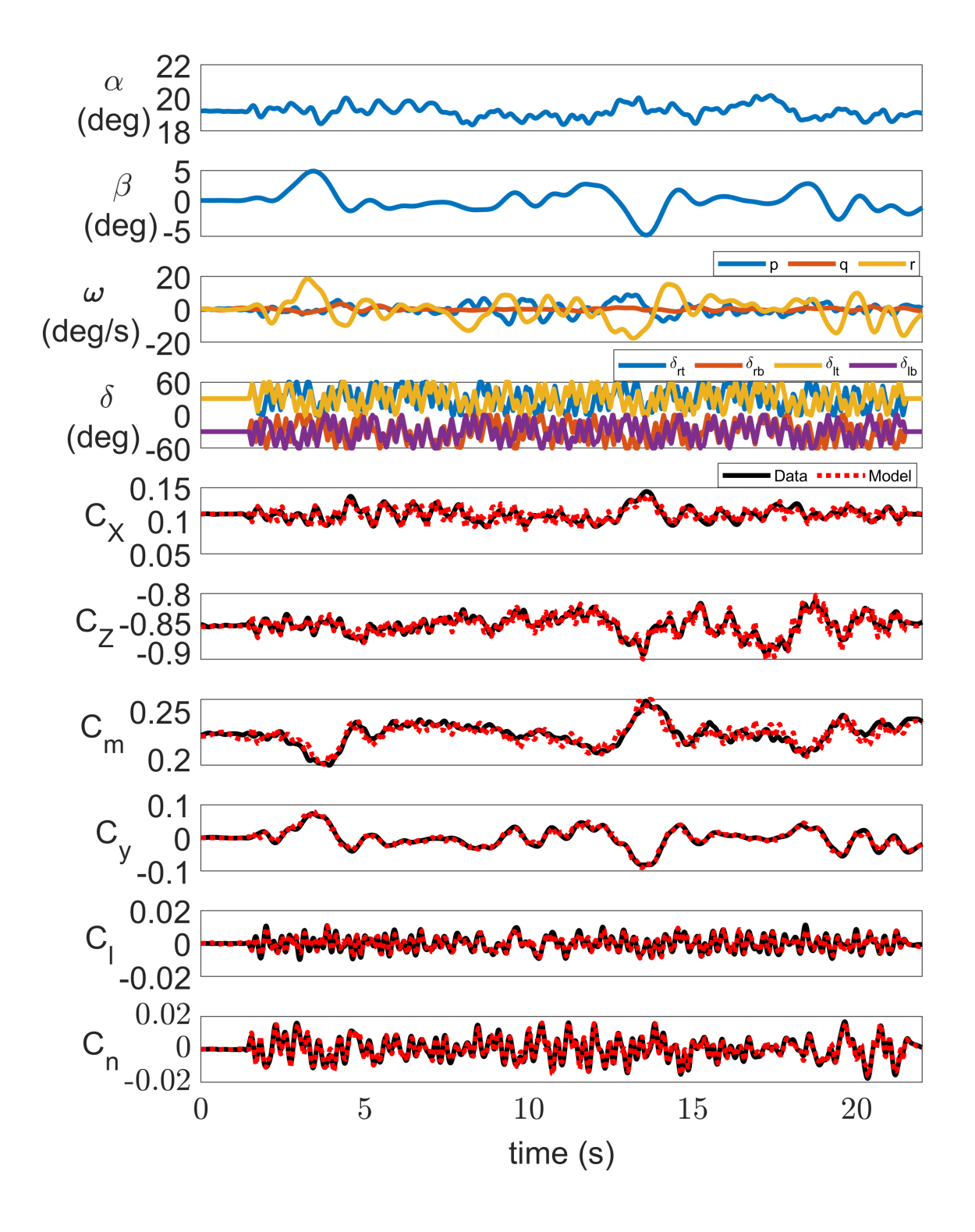


Fig. 5 Time history data for model matching.

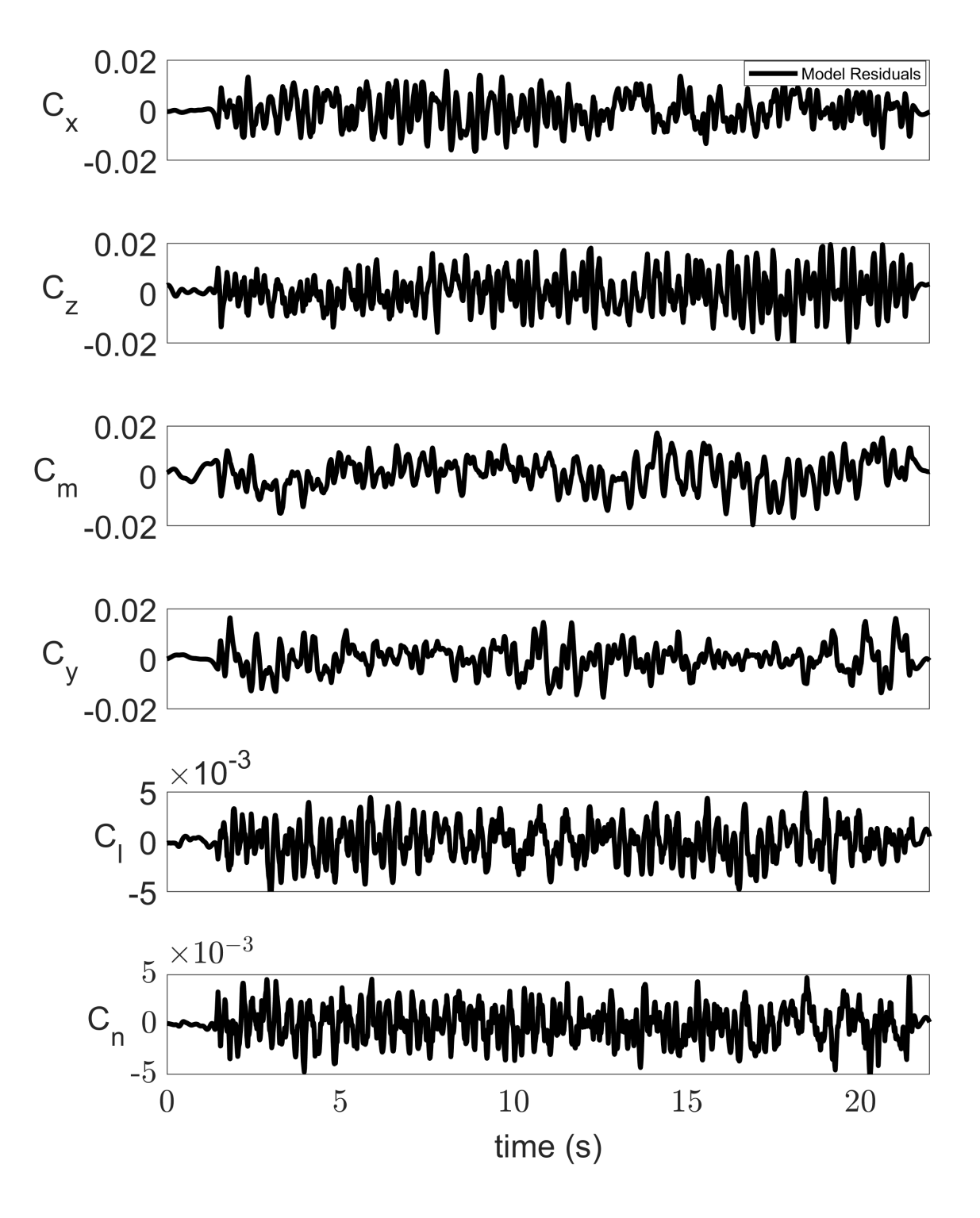


Fig. 6 Time history data for model matching residuals.

An example equation for the linear model for z-axis body vertical force coefficient is expressed as

$$C_{Z} = C_{Z_{0}} + C_{Z_{\alpha}} \Delta \alpha + C_{Z_{\beta}} \beta + C_{Z_{q}} \frac{\bar{c}}{2V_{\infty}} q + C_{Z_{\delta_{rt}}} \Delta \delta_{rt} + C_{Z_{\delta_{rb}}} \Delta \delta_{rb} + C_{Z_{\delta_{lt}}} \Delta \delta_{lt} + C_{Z_{\delta_{lb}}} \Delta \delta_{lb} \tag{5}$$

where $\Delta\alpha$ represents the perturbation of α about the mean steady-state value of 19.2 deg, and $\Delta\delta$ are flap perturbations from the mean values. Here, $\delta_r t$ and $\delta_l t$ are suction side right and left wing flaps, respectively, while $\delta_r b$ and $\delta_l b$ correspond to the pressure side right and left wing flaps, respectively. The parameter estimates, along with the standard errors, and the percent errors for C_Z and other longitudinal channels are provided in Table 2. Similar values and error estimates for the lateral-directional coefficients are presented in Table 3.

Explaining the aerodynamic coefficients for this kite required a unique approach, as they have different aspects to those of conventional aircraft. For instance, C_{Z_0} typically reflects the normalized weight of the aircraft; however, for the kite, this coefficient is affected by the presence of tether tension and the high steady-state angle of attack, making the C_{Z_0} value different from the normalized weight. Other notable differences include a relatively low $C_{Z_{\alpha}}$, which results from the slightly inefficient airfoil cross-section shape of the wing. The derivative $C_{Z_{\beta}}$, which is not usually present for fixed-wing aircraft, is also present for the kite due to the high α operational conditions, which increases the lift sensitivity to the side-slip angle. Additionally, the control derivatives of the covert flaps are also relatively low due to the low operational Reynold's number of the kite and the placement of flaps near the leading edge.

Other notable parameter estimates include a positive C_{X_0} and $C_{X_{\alpha}}$. At first glance, this may appear nonphysical in the context of traditional aircraft aerodynamics, as it suggests the possibility of negative drag. However, for the kite, which operates at significantly large angles of attack, the resolution of body-axis aerodynamic forces into the wind-axis makes it such that positive C_{X_0} and $C_{X_{\alpha}}$ are consistent with a net positive drag force.

Moreover, examining the C_m equation shows that the kite is statically unstable because the slope $C_{m_{\alpha}}$ is not negative. This instability arises because the kite is a flying wing with no tail to provide longitudinal stability. In this kite, the C_m control unit is the pitch control mechanism connecting the bridle lines to the main tether line, as shown in Fig. 1b.

Finally, the control derivatives for C_X and C_Z (or C_l and C_n) are very similar in magnitude, which is atypical for conventional aircraft that usually exhibit larger control derivatives for the flaps for C_Z (or C_l) compared to C_X (or C_n). In this case, this characteristic is intentional, as the collocated leading-edge flaps serve as the primary flight control device for the figure 8 energy harvesting maneuver. This configuration is specifically designed to primarily control yaw and has been shown to achieve this effectively, as demonstrated in [21, 22]. Regarding the lateral stability of the kite, C_{l_β} is positive, indicating that the kite is statically unstable in the rolling direction. In contrast, C_{n_β} is positive, suggesting stability in the yaw direction. The rolling instability is mitigated by the tension in the bridle lines connected to the left and right wings. For example, if the kite is perturbed right wing down (positive roll), the tension in the left-wing bridle line increases, providing a negative (restoring) rolling moment on the kite.

To improve the predictive models, a nonlinear second-order model was fitted. However, this approach did not yield a significant improvement, with R^2 values for the forces and moments increasing by only 1 to 4%. The limited enhancement may be attributed to the small perturbations in α and β observed during flight, which likely did not introduce substantial nonlinearities into the aerodynamic response. Additionally, the lack of large control surface deflections further constrained the potential for nonlinear effects. As a result, the nonlinear models are omitted from this paper.

To demonstrate the predictive power of the model, a 3211 maneuver was applied to the kite in the simulator. The time history response is shown in Fig. 7. All models exhibit validation R^2 values that are comparable to the modeling R^2 values, as presented in Table 2 and Table 3. This indicates that the models are well-fitted and not over fitted to a specific data set.

VI. Conclusions

This work highlights the potential of system identification (SysID) techniques for developing accurate aerodynamic models for tethered kite systems. In this study, SysID was applied to simulate Toyota's Airborne Wind Energy Harvesting (AWEH) kite, with the aim of estimating its aerodynamic properties and validating the proposed modeling approach. The excitation maneuvers employed orthogonal phase-optimized multisine inputs to simultaneously actuate all four control surfaces, allowing the identification of longitudinal and lateral-directional aerodynamic models. Aerodynamic force and moment coefficients were determined using a modified flight dynamics model that accounted for the bridle tension effects specific to the tethered kite configuration. Equation-error approach was used for model identification, with model structure determination and parameter estimation conducted through stepwise regression and ordinary least

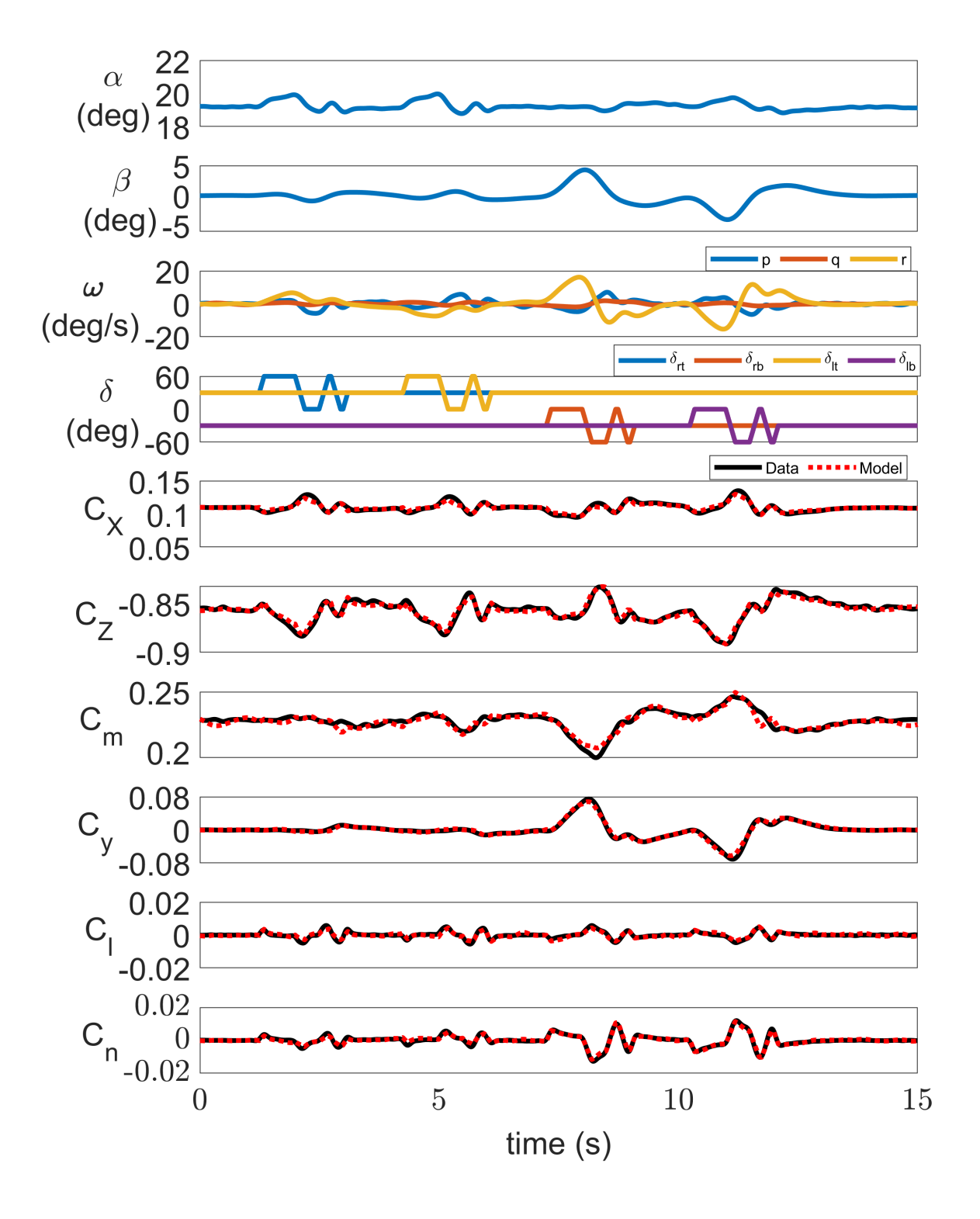


Fig. 7 Time history data for model validation.

squares, respectively. This approach ensured the efficient selection of relevant terms and enabled the quantification of uncertainties in the stability and control derivatives. Both linear and non-linear models were developed, and their predictive performance was validated using an independent 3211 maneuver.

The findings of this study can be summarized as follows:

- The multisine excitation inputs successfully excited the dynamic modes of the kite, generating data with sufficient informational content for system identification. By simultaneously actuating all control surfaces, the complete model was identified within a single maneuver, thereby reducing both testing time and associated costs. For flight testing, the same multisine inputs will be employed and iteratively refined to more effectively target specific dynamic modes, with a particular focus on improving model accuracy for pitching and rolling motions.
- Stepwise regression and the equation-error approach for parameter estimation were successfully used to match the
 identified aerodynamic models to the simulated data. This method provided the advantage of using statistical
 metrics for automatic regressor selection, ensuring a fast and efficient identification process.
- Second-order nonlinear models provided a small improvement in predictive accuracy, with an increase in R² values of 1 to 4%. Although the improvement was minimal in the simulation, larger variations in α and β during flight testing are expected to necessitate higher-order terms to capture the aerodynamic interactions of the control surfaces. Therefore, linear and non-linear models will be fitted in future flight tests.
- The overall approach demonstrated in this study will guide the planning and execution of future flight tests of
 the Mothership kite to efficiently and effectively identify its flight dynamic model. These models are critical for
 controller design and optimization.

Acknowledgments

The authors acknowledge funding from the Future Mobility Research Department at Toyota Research Institute of North America. The authors thank Dr. Jared Grauer from NASA Langley for his insights and suggestions regarding the System Identification process that helped elevate the quality of this work.

References

- [1] Bosch, A., Schmehl, R., Tiso, P., and Rixen, D., "Dynamic Nonlinear Aeroelastic Model of a Kite for Power Generation," *Journal of Guidance, Control, and Dynamics*, Vol. 37, No. 5, 2014, pp. 1426–1436. https://doi.org/10.2514/1.G000545.
- [2] Diehl, M., Airborne Wind Energy: Basic Concepts and Physical Foundations, 1st ed., Springer, New York, NY, 2013.
- [3] X, a division of Google LLC, "Harnessing Wind Energy With Kites to Create Renewable Electricity," www.x.company/projects/makani, Nov. 2024.
- [4] SkySails Marine, "Skysails Marine The Pioneer of Kite-Based Propulsion Systems," www.skysails-marine.com, Nov. 2024.
- [5] Formosa, W., Sant, T., De Marco, C., and Figari, M., "Wind-Assisted Ship Propulsion of a Series 60 Ship Using a Static Kite Sail," *Journal of Marine Science and Engineering*, Vol. 11, No. 1, 2023, p. 117. https://doi.org/10.3390/jmse11010117.
- [6] Nam, T., Itakura, E., and Tsukada, T., "High Altitude Aerial Platform 'Mothership' Project Vision and Progress," *AIAA Paper* 2024-2094, 2024. https://doi.org/10.2514/6.2024-2094.
- [7] Zhu, Y., Deng, X., Gupta, R., and Nam, T., "Navigation and Flight Control for Airborne Wind Energy Kite," AIAA Paper 2024-2097, 2024. https://doi.org/10.2514/6.2024-2097.
- [8] Toyota, "Toyota Mothership: Multifunctional Energy Harvesting Kite System," amrd.toyota.com/mothership-automated-pattern-flight, Nov. 2024.
- [9] Loyd, M., "Crosswind Kite Power (for Large-Scale Wind Power Production)," *Journal of Energy*, Vol. 4, No. 3, 1980, pp. 106–111. https://doi.org/10.2514/3.48021.
- [10] Terink, E., Breukels, J., Schmehl, R., and Ockels, W., "Flight Dynamics and Stability of a Tethered Inflatable Kiteplane," *Journal of Aircraft*, Vol. 48, No. 2, 2011, pp. 503–513. https://doi.org/10.2514/1.C031108.
- [11] Lansdorp, B., Ruiterkamp, R., Williams, P., and Ockels, W., "Modeling, Simulation, and Testing of Surf Kites for Power Generation," *AIAA Paper 2008-6693*, 2008. https://doi.org/10.2514/6.2008-6693.
- [12] Gupta, R., Zhu, Y., Nam, T., Tsukada, T., Fukagawa, T., and Itakura, E., "Cross Wind Flight Dynamics Modeling of Tethered Kite," *AIAA Paper 2022-0136*, 2022. https://doi.org/10.2514/6.2022-0136.

- [13] Morelli, E., and Klein, V., Aircraft System Identification: Theory and Practice, 2nd ed., Sunflyte Enterprises, Williamsburg, VA, 2016.
- [14] Grauer, J., and Morelli, E., "Introduction to the Advances in Aircraft System Identification from Flight Test Data Virtual Collection," *Journal of Aircraft*, Vol. 60, No. 5, 2023, pp. 1329–1330. https://doi.org/10.2514/1.C037583.
- [15] Murri, D., Morelli, E., Pei, J., Roithmayr, C., Matz, D., Barton, R., and Mendenhall, M., "Application of System Identification to Parachute Modeling," NASA TM-220410, Oct. 2019.
- [16] Grauer, J., and Boucher, M., "System Identification of Flexible Aircraft: Lessons Learned from the X-56A Phase 1 Flight Tests," AIAA Paper 2020-1017, 2020. https://doi.org/10.2514/6.2020-1017.
- [17] Morelli, E., "Multiple Input Design for Real-Time Parameter Estimation in the Frequency Domain," *International Federation of Automatic Control (IFAC)*, Vol. 36, No. 16, 2003, pp. 639–644. https://doi.org/10.1016/S1474-6670(17)34833-4.
- [18] Toyota, "TRINA Mothership," amrd.toyota.com/mothership-automated-pattern-flight, Nov. 2024.
- [19] Toyota, "Mothership project," www.toyota-global.com/innovation/partner_robot/news/202201_01.html, Nov. 2024.
- [20] Carruthers, A., Thomas, A., and Taylor, G., "Automatic Aeroelastic Devices in the Wings of a Steppe Eagle Aquila Nipalensis," Journal of Experimental Biology, Vol. 210, No. 23, 2007, pp. 4136–4149. https://doi.org/10.1242/jeb.011197.
- [21] Zekry, D., Nam, T., Gupta, R., Zhu, Y., and Wissa, A., "Covert-Inspired Flaps: an Experimental Study to Understand the Interactions Between Upperwing and Underwing Covert Feathers," *Bioinspiration & Biomimetics*, Vol. 18, No. 4, 2023, p. 046021. https://doi.org/10.1088/1748-3190/acdb1d.
- [22] Zekry, D., and Wissa, A., "The Physics of Bio-Inspired Covert Flaps As Flight Control Devices," SMASIS2024-139944, V001T06A005, 2024. https://doi.org/10.1115/SMASIS2024-139944.
- [23] Zekry, D., Duan, C., Ito, M., and Wissa, A., "Design of Experiments for Two-and Three-Dimensional Bio-Inspired Flow Control Devices," AIAA Paper 2021-0467, 2021. https://doi.org/10.2514/6.2021-0467.
- [24] Othman, A., Nair, N., Goza, A., and Wissa, A., "Feather-Inspired Flow Control Device Across Flight Regimes," Bioinspiration & biomimetics, Vol. 18, No. 6, 2023, p. 066010. https://doi.org/10.1088/1748-3190/acfa4f.
- [25] Othman, A., Zekry, D., Saro-Cortes, V., Lee, K., and Wissa, A., "Aerial and Aquatic Biological and Bioinspired Flow Control Strategies," Communications Engineering Nature, Vol. 2, No. 1, 2023, p. 30. https://doi.org/10.1038/s44172-023-00077-0.
- [26] Aeroprobe Corporation, "Aeroprobe," www.aeroprobe.com, Nov. 2024.
- [27] Nam, T., Vahid, O., Gupta, R., and Kapania, R., "High Altitude Airborne Wind Energy," AIAA Paper 2021-1815, 2021. https://doi.org/10.2514/6.2021-1815.
- [28] Grauer, J., and Boucher, M., "Identification of Aeroelastic Models for the X-56A Longitudinal Dynamics Using Multisine Inputs and Output Error in the Frequency Domain," Aerospace, Vol. 6, No. 2, 2019, p. 24. https://doi.org/10.3390/aerospace6020024.
- [29] Morelli, E., "Flight-Test Experiment Design for Characterizing Stability and Control of Hypersonic Vehicles," *Journal of Guidance, Control, and Dynamics*, Vol. 32, No. 3, 2009, pp. 94–959. https://doi.org/10.2514/1.37092.
- [30] Morelli, E., "Practical Aspects of Multiple-Input Design for Aircraft System Identification Flight Tests," AIAA Paper 2021-2795, 2021. https://doi.org/10.2514/6.2021-2795.
- [31] NASA, "System IDentification Programs for AirCraft (SIDPAC)," software.nasa.gov/software/LAR-16100-1, Nov. 2024.
- [32] Etkin, B., and Reid, L., Dynamics of Flight, 2nd ed., Wiley, New York, NY, 1959.
- [33] Grauer, J., and Morelli, E., "Dependence of Dynamic Modeling Accuracy on Sensor Measurements, Mass Properties, and Aircraft Geometry," NASA TM-218056, Nov. 2013.
- [34] SAS Institute Inc., "JMP Statistical Software," www.jmp.com, Nov. 2024.